Journal of Advanced Ceramics
2023, **12**(6): 1201–1213
https://doi.org/10.26599/JAC.2023.9220749
ISSN 2226-4108
CN 10-1154/TQ

Research Article

Fast ion-conducting high-entropy garnet solid-state electrolytes with excellent air stability

Shaoxiong Han[a,b], Ziqi Wang[a,b], Yue Ma[a,b], Yang Miao[a], Xiaomin Wang[a], Yong Wang[a,b,*], Yongzhen Wang[a,b,*]

[a]*College of Materials Science and Engineering, Taiyuan University of Technology, Taiyuan 030024, China*
[b]*Shanxi Joint Laboratory of Coal based Solid Waste Resource Utilization and Green Ecological Development, Taiyuan 030024, China*

Received: December 20, 2022; Revised: March 15, 2023; Accepted: April 1, 2023

Abstract: The garnet-type electrolyte is one of the most promising solid-state electrolytes (SSEs) due to its high ionic conductivity (σ) and wide electrochemical window. However, such electrolyte generates lithium carbonate (Li_2CO_3) in air, leading to an increase in impedance, which greatly limits their practical applications. In turn, high-entropy ceramics (HECs) can improve phase stability due to high-entropy effect. Herein, high-entropy garnet (HEG) $Li_{6.2}La_3(Zr_{0.2}Hf_{0.2}Ti_{0.2}Nb_{0.2}Ta_{0.2})_2O_{12}$ (LL(ZrHfTiNbTa)O) SSEs were synthesized by the solid-state reaction method. X-ray diffraction (XRD), X-ray photoelectron spectroscopy (XPS), electrochemical impedance spectroscopy (EIS), and scanning electron microscopy (SEM) characterizations indicated that the LL(ZrHfTiNbTa)O electrolyte has excellent air stability. Room-temperature conductivity of LL(ZrHfTiNbTa)O can be maintained at ~1.42×10^{-4} S/cm after exposure to air for 2 months. Single-element-doped garnets were synthesized to explain the role of different elements and the mechanism of air stabilization. In addition, a lithium (Li)/LL(ZrHfTiNbTa)O/Li symmetric cell cycle is stable over 600 h, and the critical current density (CCD) is 1.24 mA/cm^2, indicating remarkable stability of the Li/LL(ZrHfTiNbTa)O interface. Moreover, the $LiFePO_4$/LL(ZrHfTiNbTa)O/Li cell shows excellent rate performance at 30 ℃. These results suggest that HECs can be one of the strategies for improving the performance of SSEs in the future due to their unique effects.

Keywords: solid-state batteries; high-entropy ceramics (HECs); garnet electrolytes; air stability

1 Introduction

Lithium (Li) batteries are widely used in various electronic devices due to their high operating voltages, high energy densities, and long cycle lives [1]. However, most of the actual commercial batteries are organic liquid electrolyte-dominated Li-ion batteries. Although liquid electrolytes possess high Li-ion conductivity and good wetting for electrodes, critical safety issues [2] such as short-circuiting, easy leakage, corrosion, and flammability have limits on their widespread practical applications and development. In

* Corresponding authors.
E-mail: Yong Wang, wangyong01@tyut.edu.cn;
Yongzhen Wang, wangyongzhen@tyut.edu.cn

view of this, all-solid-state lithium batteries (ASSLBs) have attracted considerable attention from Sun *et al*. [3], Wang *et al*. [4], and He *et al*. [5] because of their high safety, high-temperature stability, and high potential energy density. ASSLBs are designed using solid electrolytes instead of liquid electrolytes. Since the performance of a solid-state battery depends on the solid electrolyte, extensive research in the past decades has been devoted to developing new types of solid electrolytes, such as NASICON [6,7], LISICON [8], perovskite [9], and garnet-type [10] electrolytes.

$Li_7La_3Zr_2O_{12}$ (LLZO) is a type of Li-stuffed garnet, which has been considered a promising solid-state electrolyte (SSE) for the batteries with high lithium ionic conductivity (σ), wide electrochemical window, excellent mechanical strength, and safety [11]. However, experiments have revealed that garnet electrolytes are unstable and prone to reaction with H_2O and CO_2 in air [12]. A more widely accepted reaction pathway includes two steps. First, moisture in air reacts with LLZO to form LiOH by the Li^+/H^+ ion exchange [13].

$$Li_7La_3Zr_2O_{12} + xH_2O \rightarrow Li_{7-x}H_xLa_3Zr_2O_{12} + xLiOH \quad \text{Reaction (1)}$$

LiOH subsequently reacts with CO_2 to form lithium carbonate (Li_2CO_3) on the surface of the garnet :

$$LiOH + \frac{1}{2}CO_2 \rightarrow \frac{1}{2}Li_2CO_3 + \frac{1}{2}H_2O \quad \text{Reaction (2)}$$

Therefore, it is necessary to increase the stability of the garnet-type SSEs against moisture and CO_2 in air. Up till now, many attempts have been made to improve the air stability of the garnet-type SSEs. For instance, Abrha *et al*. [14] synthesized dual-doped (Ga,Nb)–LLZO and compared it with previously reported (Ca,Nb)–LLZO garnets [15], concluding that (Ga,Nb)–LLZO have better air stability. Moreover, no Li_2CO_3 impurities were found in the as-prepared (Ga,Nb)–LLZO garnet within a period of 7 d. The improved (Ga,Nb)–LLZO stability in air can be attributed to the doping site difference of Ca and Ga. Jia *et al*. [16] synthesized an air-stable layer on the surface of $Li_{6.6}La_3Zr_{1.6}Ta_{0.4}O_{12}$ (LLZTO) via a chemical treatment of dopamine at room temperature. It was found that dopamine-based shells on LLZTO particles resist air attack for up to 20 d. Wang *et al*. [17] demonstrated high-temperature thermal pulse technique for the rapid ceramic surface processing for the first time, which allowed to eliminate Li_2CO_3 contaminations from LLZO surfaces in less than 2 s. The method consisted of high-energy laser beam absorption by surface impurities to remove them from a LLZO substrate by the rapidly expanding plasma.

High-entropy ceramics (HECs) are solid solution of inorganic compounds with one or more Wyckoff sites shared by equal or near-equal atomic ratios of multi-principal elements [18]. HECs have many outstanding advantages over single-phase ceramics, such as high densities [19]. This is because the packing density of atoms increases due to a distinct atomic radius. For example, $(Hf_{0.2}Zr_{0.2}Ta_{0.2}Nb_{0.2}Ti_{0.2})B_2$ and (Hf,Zr,Ti,Ta,Nb)C ceramics were synthesized with a relative density of ~99% [20,21]. Reference [22] shows that increasing the relative density can improve the air stability of the garnet electrolytes. In addition, there is a cocktail effect, where the synergistic effect of different elements can yield unexpected performance [18]. Hence, the synthesis of high-entropy garnets (HEGs) is expected to solve the issues of LLZO, such as low-temperature cubic to tetragonal phase transition [23], poor air stability, and low mechanical strength [24].

In this work, we introduced high entropy into the LLZO solid electrolyte. Specifically, based on the first-principles calculation data from Ref. [25], the HEG electrolyte $Li_{6.2}La_3(Zr_{0.2}Hf_{0.2}Ti_{0.2}Nb_{0.2}Ta_{0.2})_2O_{12}$ (LL(ZrHfTiNbTa)O) was successfully synthesized by inserting five elements with an equal molar ratio at the Zr site. Compared with that of LLZO, the air stability of LL(ZrHfTiNbTa)O is substantially improved. The ionic conductivity of LL(ZrHfTiNbTa)O measured at 25 ℃ is ~1.42×10^{-4} S/cm and remains constant for 60 d. Also, single-element-doped garnets were synthesized to explain the role of different elements and the mechanism of air stabilization. Besides, the introduction of high entropy noticeably increased Li^+ transference number (TN), critical current density (CCD), and rate performance of lithium batteries.

2 Materials and methods

2.1 Preparation of LLZO and LL(ZrHfTiNbTa)O pellets

First, LLZO powders were prepared by Ref. [26]. The LL(ZrHfTiNbTa)O powders were obtained by the traditional solid-state reaction method. For this purpose, Li_2CO_3 (99.99%, with a 10% lithium excess to compensate for lithium loss, Aladdin), La_2O_3 (99.95%, Aladdin), ZrO_2 (99.99%, Aladdin), HfO_2 (99%, Aladdin), TiO_2 (99.99%, Aladdin), Nb_2O_5 (99.9%, Aladdin), and

Ta_2O_5 (99.5%, Aladdin), all taken in a stoichiometric ratio, were mixed in a zirconia ball mill tank (YXQM-4L, Changsha Miqi Instrument) with 2-propanol as grinding media to obtain the mixed slurry after ball milling at 400 r/min for 12 h [27]. The slurry was dried in an oven (DZF-6020, Hefei Kejing Materials Technology Co., Ltd.) at a controlled temperature of 80 ℃ for 6 h to produce the powders. The powders were calcined in a muffle furnace (KSL-1400X-A1, Hefei Kejing Materials Technology Co., Ltd.) at temperatures of 750–1100 ℃ for 5 h to get LL(ZrHfTiNbTa)O mother powders. Next, the powders were mixed with 2 wt% polyvinyl butyral (PVB) binder and pressed into green pellets under a pressure of 6 MPa [28]. The pellets were then sintered in a muffle furnace at 1250 ℃ for 5 h and finally polished with 400, 800, 1200, 2500, and 3000 mesh sandpapers [29]. The same procedure was conducted concerning the LLZO powders to obtain LLZO pellets. Moreover, various single-element-doped garnet electrolytes ($Li_{6.6}La_3Zr_{1.6}Ta_{0.4}O_{12}$ (LLZTO), $Li_{6.6}La_3Zr_{1.6}Nb_{0.4}O_{12}$ (LLZNO), $Li_7La_3Zr_{1.6}Ti_{0.4}O_{12}$ (LLZTiO), and $Li_7La_3Zr_{1.6}Hf_{0.4}O_{12}$ (LLZHO)) were prepared using the same method.

2. 2 Characterizations and measurements

Crystal structures of LLZO and LL(ZrHfTiNbTa)O particles were examined by an X-ray diffractometer (D2 Phaser, Bruker). Morphologies of specimens were inspected via a scanning electron microscope (MIRA LMS, TESCAN) at an accelerating voltage of 5 kV. The corresponding energy-dispersive X-ray spectroscopy (EDS; Xplore) elemental mappings were also carried out. An X-ray photoelectron spectrometer (K-Alpha, Thermo Scientific) and an Raman spectrometer (LabRAM HR Evolution, HORIBA Scientific) were conducted to analyze compositions of the LLZO and LL(ZrHfTiNbTa)O pellets after aging in air. Thermogravimetric analysis (TGA) and differential scanning calorimetry (DSC) curves were obtained using a TGA instrument (STA 449 F5, NETZSCH). Prior to inductively coupled plasma optical emission spectroscopy (ICP-OES; Avio 500, PerkinElmer) analysis, about each sample of 20 mg was dissolved in nitric acid of 5 mL, hydrochloric acid of 1 mL, and hydrofluoric acid of 1 mL at 493 K for 30 min in a microwave oven.

2. 3 Impedance measurement

Alternating current (AC) impedance measurements were conducted to measure ionic conductivity using an electrochemical workstation (1260+1287, Solartron) at frequencies ranging from 1 MHz to 0.1 Hz [30]. The activation energy (E_a) was performed by investigating temperature dependence in the range from –20 to 80 ℃ using the electrochemical workstation. The Ag layers were coated onto both sides of the polished pellets for lithium-ion conductivity measurements [31].

2. 4 Air stability test

LLZO and LL(ZrHfTiNbTa)O ceramic pellets were labeled as LLZO-fresh, LL(ZrHfTiNbTa)O-fresh, LLZO-*n*d, and LL(ZrHfTiNbTa)O-*n*d (n = 10, 20, 30, 40, 50, and 60). To compare their air stability, the LLZO and LL(ZrHfTiNbTa)O pellets were aged in air at relative humidity of ~45%. The pellets were then subjected to X-ray diffraction (XRD), scanning electron microscopy (SEM), X-ray photoelectron spectroscopy (XPS), and electrochemical impedance spectroscopy (EIS) tests every 10 d [14,16]. The air stability of the LLZO and LL(ZrHfTiNbTa)O pellets through changes in phase, morphology, and impedance were compared. In addition, impedance parameters of LLZTO, LLZNO, LLZTiO, and LLZHO were studied for 5 consecutive days.

2. 5 Cell assembly and electrochemical measurements

Linear sweep voltammetry (LSV) and cyclic voltammetry (CV) curves were acquired using stainless steel (SS)/garnet/Li 2032-type coin cells. The curves were recorded in a voltage ranging from 2 to 6 V and from 0 to 4 V at a scan rate of 5 mV/s. The Li/garnet/Li symmetric cells were assembled to test the cycle performance and ion TN. The full cells were assembled in a lithium iron phosphate (LFP)/garnet/Li configuration. Li metal foils with a diameter of 15 mm were used as anodes, and commercial LFP polar tablets (loading: 10.5 mg/cm^2) with a diameter of 14 mm were taken as cathodes. The thickness and diameter of the garnet electrolyte were ~800 μm and ~16 mm, respectively. The full cells were charged and discharged between 2.7 and 4.2 V vs. Li/Li$^+$ under various current densities. $LiPF_6$ (1 M) in the mixture of ethylene carbonate (EC) and diethyl carbonate (DEC) (V(EC) ∶ V(DEC) = 1 ∶ 1) was used to wet the Li/garnet, SS/garnet, and LFP/garnet interfaces [32].

2. 6 Hardness test

Vickers microhardness tests were carried out conforming to American Society for Testing Material (ASTM)

C1327 standard on a diamond micro indenter (HVS-1000A, Hitachi) at a standard loading force of 9.8 N and holding time of 15 s. Ten measurements were conducted at different locations for each specimen to ensure statistical validity [33].

3 Results and discussion

3. 1 Synthesis of pure LL(ZrHfTiNbTa)O

Figure 1 displays XRD patterns of a LL(ZrHfTiNbTa)O precursor calcined at different temperatures. The precursor calcined at 750 ℃ for 5 h exhibited a garnet cubic phase structure, but there was also an impurity peak at 2θ = 22.4°, which should be attributed to lanthanum niobium oxides ($La_{0.33}NbO_3$, PDF#36-0126) that were not fully reacted. The result was consistent with the phase transition temperature data obtained by a DSC curve (Fig. S1 in the Electronic Supplementary Material (ESM)). After calcination at 900 ℃ for 5 h, a standard cubic phase structure was formed. Therefore, the temperature of 900 ℃ and the calcination time of 5 h were the most optimal synthesis conditions of LL(ZrHfTiNbTa)O. As a control, the LLZO precursor was calcined at 900 ℃ at different time. As shown in Fig. S2 in the ESM, LLZO calcined at 900 ℃ for 5 h possessed a tetragonal phase structure, and the further extension of the calcination time to 12 h caused the formation of the cubic phase. These results indicate that high-entropy doping can promote the tetragonal-to-cubic phase transition [34]. Miara *et al*. [25] applied the density functional theory (DFT) to calculate defect energy and site preference of all possible dopants in lithium garnets. As shown in Fig. S3 in the ESM, the

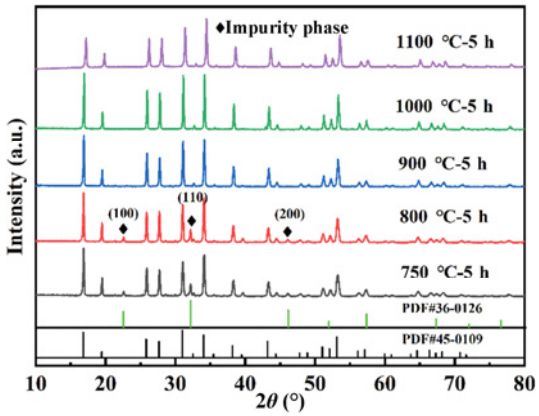

Fig. 1 XRD patterns of LL(ZrHfTiNbTa)O precursor calcined at different temperatures.

color shows the most stable cation site (green for the Li site, red for the La site, and blue for Zr site). The darker colors signify lower defect energy. The corresponding ionic radii and coordination numbers of these five elements (zirconium (Zr), hafnium (Hf), titanium (Ti), niobium (Nb), and tantalum (Ta)) are listed in Table S1 in the ESM. All five kinds of ions have a similar radius and the same coordination number. In summary, it was established that dopants were settled at the Zr sites.

The EDS elemental mappings (Fig. 2) show uniform distributions of Zr, Hf, Ti, Nb, and Ta elements in LL(ZrHfTiNbTa)O. Suggesting that there were no obvious segregations or second phase detected, the findings were consistent with the conclusion drawn based on the XRD patterns [35]. Table 1 depicts ICP-OES data, revealing that the five elements are close to the equimolar ratio. In summary, according to the XRD patterns, EDS mappings, and ICP-OES results, HEG SSEs were successfully synthesized.

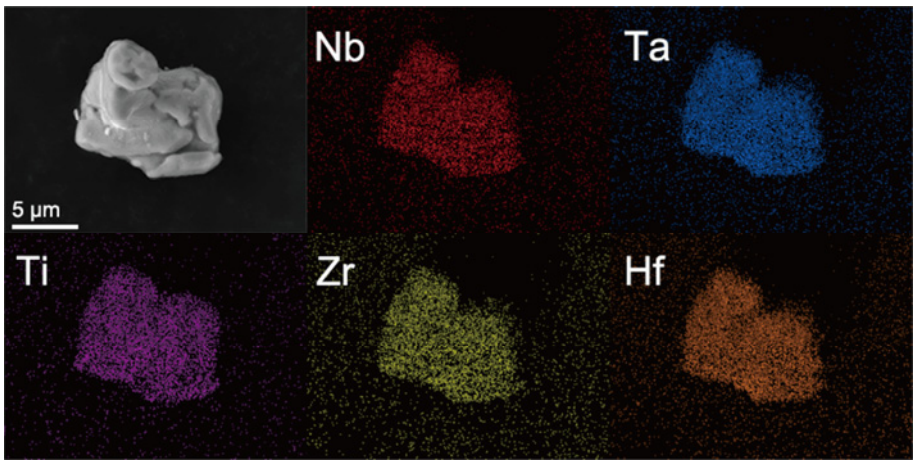

Fig. 2 EDS mappings of LL(ZrHfTiNbTa)O SSE.

Table 1 ICP-OES results of LL(ZrHfTiNbTa)O

Element	Zr	Ti	Hf	Nb	Ta
C (μg/L)	5.677	4.037	12.302	7.639	15.007
Atomic percent (%)	17	22	19	21	21

3. 2 Electrochemical impedance

Figure S4 in the ESM depicts EIS plots of the LL(ZrHfTiNbTa)O pellets at different sintering temperatures and time, implying that the lowest impedance was achieved for the pellet sintered at 1250 ℃ for 5 h. Figure 3(a) shows EIS curves of LLZO and LL(ZrHfTiNbTa)O SSEs measured at 25 ℃. In the case of LLZO, a quasi-semicircle in a high-frequency region and a tail in a low-frequency part were observed. The fitted circuit is a $R_b(R_{gb}Q_{gb})(R_{el}Q_{el})$ model, where R is the resistance, Q is the constant phase element, and the subscripts b, gb, and el refer to the contributions of the bulk, the grain boundary, and the electrode, respectively [36]. Due to a high response frequency of the grains (> 1 MHz), there were only semicircles corresponding to grain boundaries in LLZO. The value of the real part of the inflection point in the semicircle and the straight line is R of the LLZO ceramics [37]. Because of small impedance and thickness of the LL(ZrHfTiNbTa)O electrolyte pellet, the bulk grain boundary impedance value and grain boundary capacitive reactance were low, and the grain boundary semicircle disappeared, so that the EIS curve exhibited only a tail of 45° [38]. AC impedance data were further collected on the LL(ZrHfTiNbTa)O pellets of different thicknesses. As shown in Fig. S5 in the ESM, Nyquist plots' semicircles became increasingly obvious with the increase in the LL(ZrHfTiNbTa)O pellet thickness (L). Thus, the real part of the starting point of the curve is used as the total impedance value of the LL(ZrHfTiNbTa)O pellets. The σ was determined by Eq. (1):

$$\sigma = \frac{L}{RS} \tag{1}$$

where S is the active electrode area. The ionic conductivity of LL(ZrHfTiNbTa)O and LLZO were 1.42×10^{-4} and 4.17×10^{-6} S/cm, respectively. This result could be attributed to the relative densities of the ceramic pellets. According to SEM images (Fig. 4), the grains of the LL(ZrHfTiNbTa)O ceramics (Fig. 4(e)) are more tightly bound than those in the LLZO ceramics (Fig. 4(a)), which would have greatly reduced R_{gb} of the LL(ZrHfTiNbTa)O ceramics [39]. Besides, the pentavalent element doping (Ta and Nb) into LLZO can further enhance room-temperature conductivity

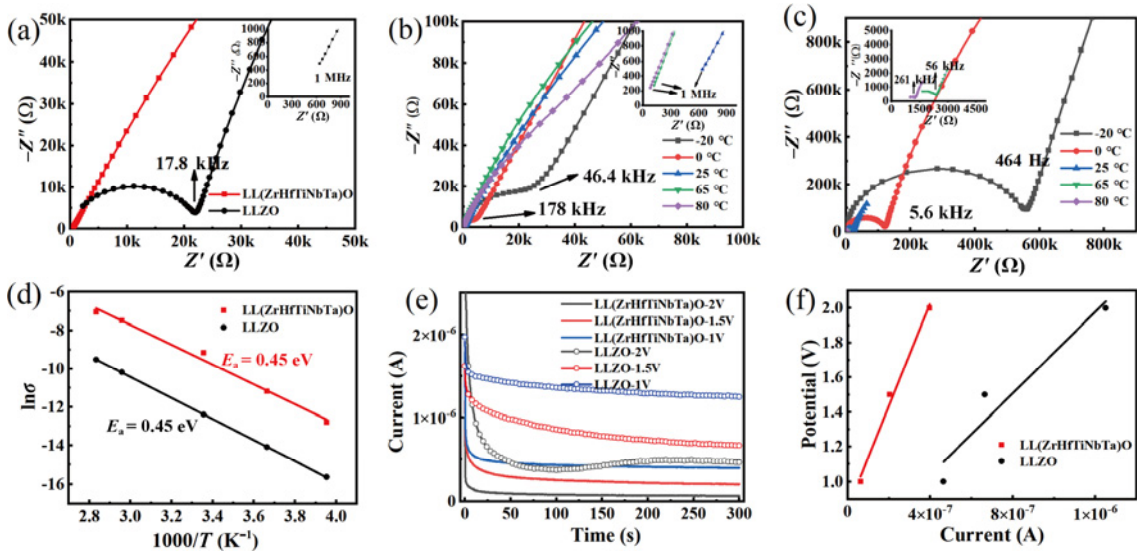

Fig. 3 (a) Nyquist plots of LL(ZrHfTiNbTa)O and LLZO pellets measured at 25 ℃ where Z' refers to the real impedance part of the AC impedance response of the electrochemical system related to ion transport, which usually corresponds to the diffusion process of ions in the electrolyte, and $-Z''$ refers to the imaginary impedance part related to the electrode surface reaction in the AC impedance response of the electrochemical system, which usually corresponds to the electron transfer process. (b) Nyquist plots of LL(ZrHfTiNbTa)O pellet measured at different temperatures. (c) Nyquist plots of LLZO measured at different temperatures. (d) Arrhenius plots of LL(ZrHfTiNbTa)O and LLZO where T is the absolute temperature. The insets show magnified high-frequency plots. (e) DC polarization curves of garnet under applied voltages of 1–2 V at 25 ℃. (f) Relationship between applied potential and constant current.

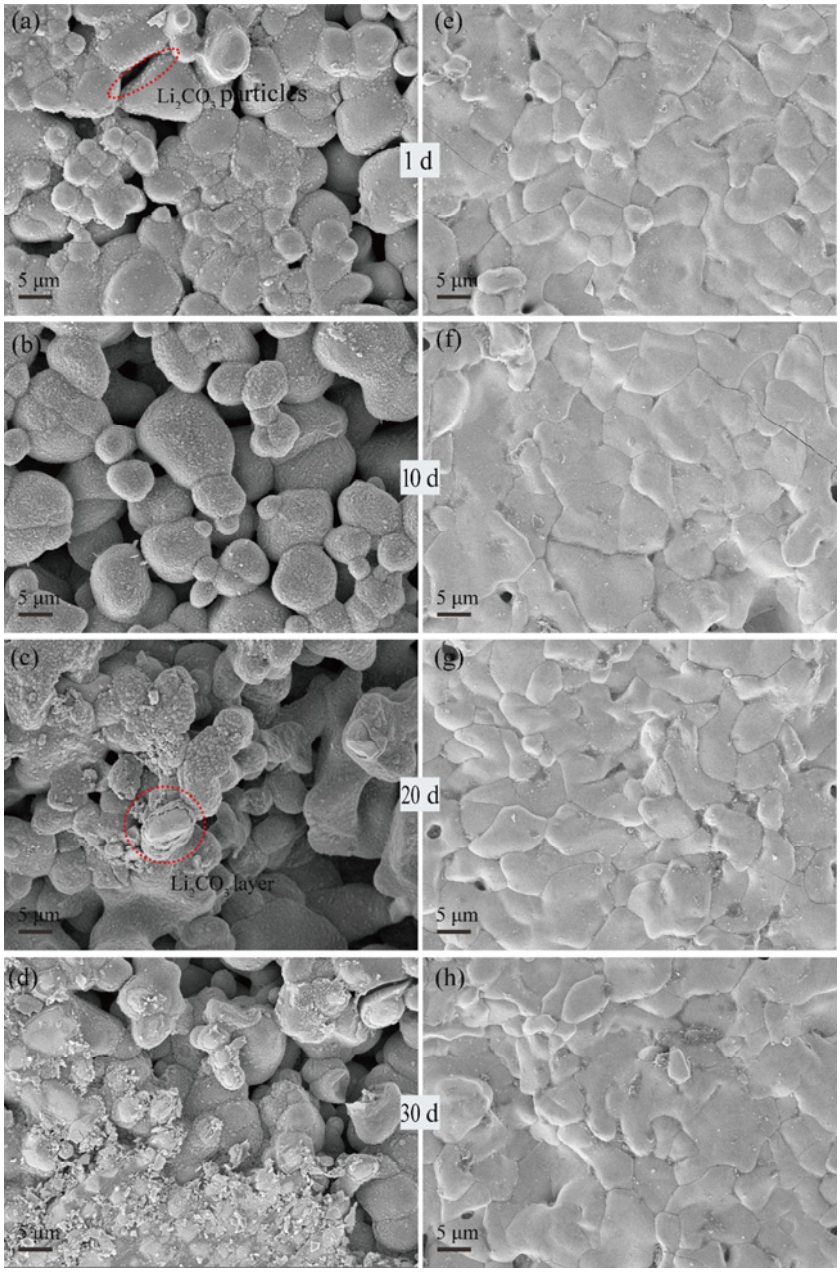

Fig. 4 SEM images of (a–d) LLZO and (e–h) LL(ZrHfTiNbTa)O pellets exposed to air for 30 d.

because of the increased amount of Li^+ vacancies as hopping sites [40]. In addition, E_a of Li^+ migration in the pellets was determined by Eq. (2) [41]:

$$\sigma = A\exp\left(\frac{-E_a}{K_b T}\right) \tag{2}$$

where A is the pre-exponential factor (a constant with the same unit as σ), T is the absolute temperature, and K_b is the Boltzmann constant. Figures 3(b) and 3(c) display EIS curves of the LL(ZrHfTiNbTa)O and LLZO electrolytes recorded at different temperatures, respectively. The E_a values of LL(ZrHfTiNbTa)O and LLZO are 0.45 and 0.47 eV, respectively (Fig. 3(d)). The electronic conductivity of LL(ZrHfTiNbTa)O and LLZO measured by the direct current (DC) polarization method were 2.33×10^{-8} and 9.22×10^{-8} S/cm, respectively. As shown in Fig. 3(e), three constant potential polarizations were applied for test accuracy, and the electronic resistances of the electrolytes are obtained by plotting standard curves (Fig. 3(f)) [42].

3.3 Air stability

Figure 4 shows morphological changes of the LLZO (Figs. 4(a)–4(d)) and LL(ZrHfTiNbTa)O (Figs. 4(e)–4(h))

pellets aged in air for 30 d. The Li_2CO_3 particles appeared on a smooth surface of LLZO after 1 d of exposure to air. Within 10 d, the number of the Li_2CO_3 particles increased. After 20 d, the Li_2CO_3 layers could be seen. Compared with LLZO, no Li_2CO_3 impurities were observed on the surface of the LL(ZrHfTiNbTa)O electrolyte. This result indicated that the air stability of LL(ZrHfTiNbTa)O is better than that of LLZO. Because LLZO possessed high porosity, H_2O and CO_2 would have entered pores and contaminated the interior in addition to eroding the surface. Furthermore, the macro morphology changes occurred in the LLZO and LL(ZrHfTiNbTa)O electrolyte pellets within 3 months, as shown in Fig. S6 in the ESM. Moreover, the apparent corroding appeared on the LLZO surface exposed to air for 60 d. After 90 d, the LLZO pellet was completely transformed into powders. On the contrary, no alteration was observed in the macroscopic morphology of the LL(ZrHfTiNbTa)O pellet within 3 months.

To quantitatively compare the relative densities of the LL(ZrHfTiNbTa)O and LLZO pellets, the volume densities (ρ_v) of the samples were determined via Archimedes method by Eq. (3):

$$\rho_v = \rho_l \frac{W_d}{W_w - W_s} \tag{3}$$

where ρ_l is the density of the liquid, and W_d, W_w, and W_s are the dry weight, the wet weight, and the suspended weight, respectively. Rietveld refinement of the XRD peaks using the GSAS package software [4] was conducted to determine the theoretical density of LL(ZrHfTiNbTa)O. Figure 5 displays the good coincidence between the observed and refined patterns with a goodness of fit (GOF) value of 2.2 and an R_{wp} value of 5.9 where R_{wp} refers to the weighted residual average. The relative densities of LL(ZrHfTiNbTa)O and LLZO (Table 2)

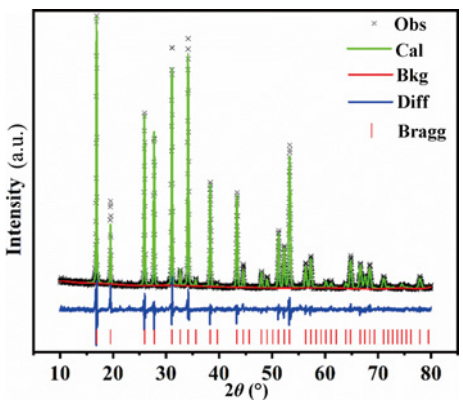

Fig. 5 Example of Rietveld refinement of LL(ZrHfTiNbTa)O based on the structural model of LLZO.

Table 2 ρ_v, theoretical densities, and relative densities of LLZO and LL(ZrHfTiNbTa)O

Sample	ρ_v (g/cm³)	Theoretical density (g/cm³)	Relative density
LLZO	2.699	5.013	53.8%
LL(ZrHfTiNbTa)O	4.963	5.499	90.3%

are 90.3% and 53.8%, respectively. Therefore, the excellent morphology stability of LL(ZrHfTiNbTa)O was attributed to its high relative density.

To further identify air pollution resistance of the LL(ZrHfTiNbTa)O and LLZO ceramic pellets, Li_2CO_3 components of the LL(ZrHfTiNbTa)O and LLZO pellets were detected by the XRD patterns and XPS spectra, as shown in Figs. 6(a)–6(c). In the XRD patterns of the LL(ZrHfTiNbTa)O pellet (Fig. 6(a)), no Li_2CO_3 was detected after 30 d. However, the obvious characteristic peak of Li_2CO_3 at 21° emerged after LLZO was aged in air for 30 d. In the C 1s spectra of the LLZO-10d specimen (Fig. 6(b)), the peaks at approximately 288.9 and 290.0 eV corresponded to carboxy impurities and carbonate species, respectively [16]. However, no carbonate peak at 290.0 eV was observed in LL(ZrHfTiNbTa)O. Moreover, there was an additional metal oxide peak at 529.4 eV in the O 1s spectra of the LL(ZrHfTiNbTa)O-10d pellet (Fig. 6(d)) [43], while only a peak of 531.8 eV was identified in the LLZO-10d sample, which was attributed to a Li_2CO_3 surface layer. The existence of Li_2CO_3 in the LLZO-10d pellet was also evident from Raman spectra (Fig. S7 in the ESM), in which the intense peak at 1100 cm^{-1} was related to the vibrations of carbonate groups [44]. However, no Li_2CO_3 traces were found in LL(ZrHfTiNbTa)O after 10 d of exposure, meaning that LL(ZrHfTiNbTa)O has remarkable phase stability in air.

A comparative impedance study of the LL(ZrHfTiNbTa)O and LLZO pellets after exposure to ambient air was performed as well. Figures 6(d) and 6(e) depict EIS spectra of the LL(ZrHfTiNbTa)O and LLZO specimens, respectively. According to the results, the impedance of LL(ZrHfTiNbTa)O barely changed within 60 d. In contrast, the impedance of LLZO was constantly increasing, being twice the initial value after 60 d. As seen in Fig. 6(f), σ of LL(ZrHfTiNbTa)O tended to be stable over 2 months, while that of LLZO exhibited an obvious declining trend. This is because Li_2CO_3 is a highly resistant phase that hinders the Li^+ transport and reduces ionic conductivity. As shown in Table S2 in the ESM, many modification methods

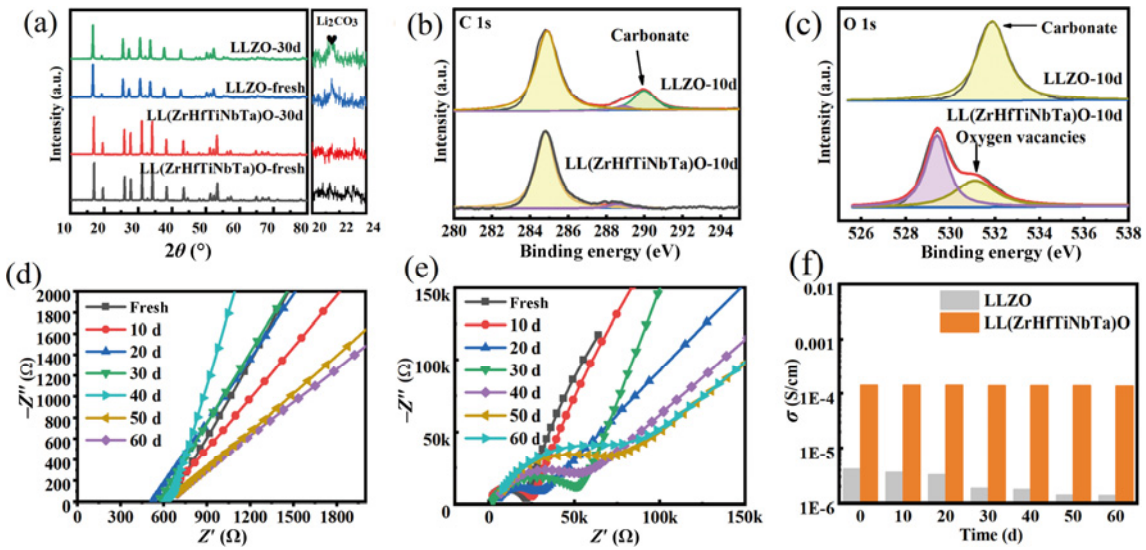

Fig. 6 (a) XRD patterns, (b, c) XPS spectra, (d, e) impedance changes, and (f) σ as a function of exposure time observed in LL(ZrHfTiNbTa)O and LLZO pellets.

allow one to improve air stability, and the effect of high-entropy doping is prominent.

To further determine the role of different elements and mechanism of LL(ZrHfTiNbTa)O air stabilization, the impedance changes of four electrolytes (LLZTO, LLZNO, LLZTiO, and LLZHO) were monitored for more than 5 d. As shown in Figs. 7(b) and 7(c), Ta and Nb doping significantly reduced the impedance of LLZO, but increased the impedance values of LLZTO and LLZNO by 206% and 331% after 5 d of exposure, respectively. The results reveal that Ta and Nb doping can improve the ionic conductivity but not the air stability. As shown in Fig. 7(d), the Ti doping of LLZO doubled its ionic conductivity and only increased the impedance by 8% after 5 d. Therefore, Ti doping enhances the ionic conductivity and air stability of LLZO. However, as seen in Fig. 7(e), the impedance of the garnet increased instead after Hf doping, probably because of the strong interaction between Hf and lithium, which hindered the migration of lithium ions [45]. As shown in Fig. 8, after 30 d, a large number of layered Li_2CO_3 contamination layers appeared on the surfaces of LLZNO and LLZTO (Figs. 8(c) and 8(d), respectively). In contrast, only a small amount of chain beads of Li_2CO_3 appeared on the surfaces of LLZHO and LLZTiO (Figs. 8(a) and 8(b), respectively).

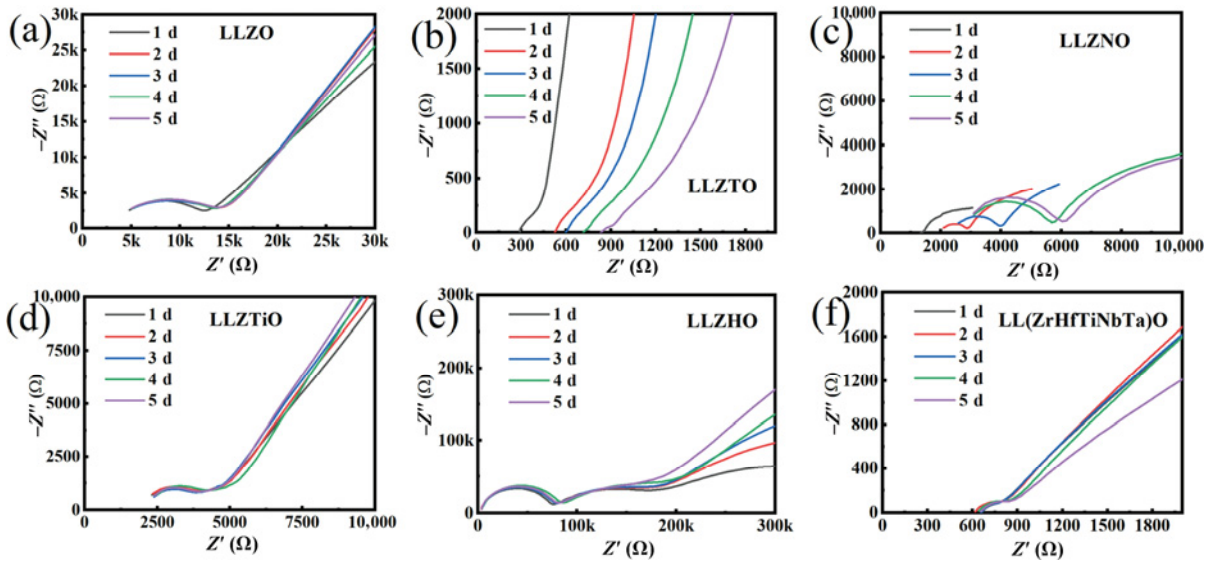

Fig. 7 EIS evolution of (a) LLZO, (b) LLZTO, (c) LLZNO, (d) LLZTiO, (e) LLZHO, and (f) LL(ZrHfTiNbTa)O after exposure to air.

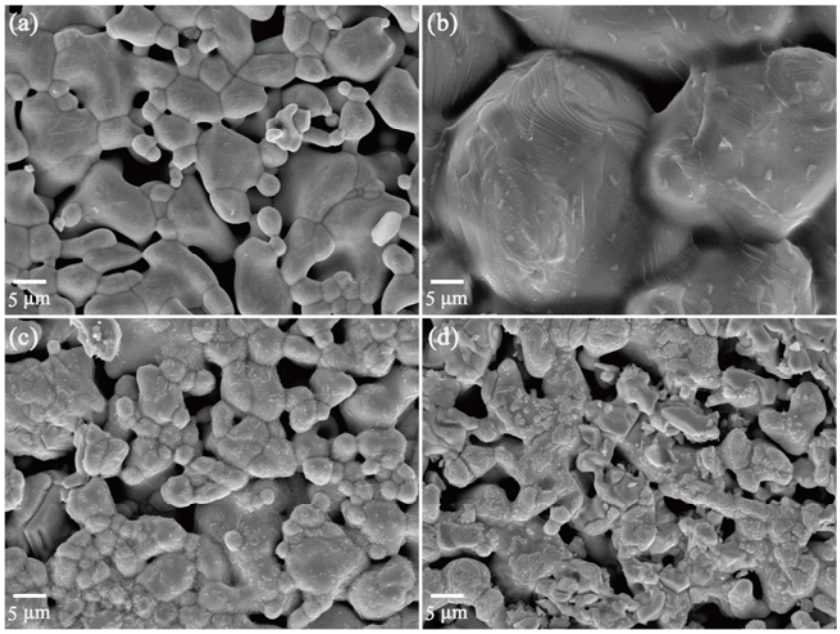

Fig. 8 SEM images of (a) LLZHO, (b) LLZTiO, (c) LLZNO, and (d) LLZTO pellets exposed to air for 30 d.

As shown in Fig. 9(a), melting points of different garnets were tested by the DSC curves, and LLZTiO had the lowest melting point, indicating that Ti doping could promote the sintering of electrolyte pellets. The TGA curves (Fig. 9(b)) show three weight-loss steps: the evaporation of water molecules absorbed at the surface at 250 ℃ (Step I), the escape of H^+ as H_2O at 400–500 ℃ (Step II), and the decomposition of the carbonate by-products at 500–800 ℃ (Step III). The percentage of H^+/Li^+ exchange is quantified according to the weight loss in Step II [46]. LLZHO has no weight loss in Step II, indicating that Hf can effectively slow down the process of H^+/Li^+ exchange [47]. Also, we found that the proton exchange process of the garnet electrolyte is slow for single-element doping with high impedance, probably because a strong force of the doped atom on Li^+ hinders its migration.

In summary, the doping of Ta and Nb can improve the ionic conductivity, the doping of Ti can promote the sintering of the electrolyte pellets to improve the densities, and the doping of Hf can inhibit the H^+/Li^+ exchange to improve the air stability. Under the synergistic effect of the Ta, Nb, Ti, and Hf elements, the LL(ZrHfTiNbTa)O pellet exhibits both high ionic conductivity and outstanding air stability.

3.4 Electrochemical properties

To test and compare the practicality of LL(ZrHfTiNbTa)O and LLZO, their electrochemical properties were evaluated as well. Figure 10(a) illustrates electrochemical windows of the LL(ZrHfTiNbTa)O and LLZO electrolytes. The LL(ZrHfTiNbTa)O one was electrochemically stable up to 4.6 V, which indicated its suitability for high-voltage solid lithium batteries [48]. Meanwhile, CCD of a Li/LL(ZrHfTiNbTa)O/Li symmetric cell was

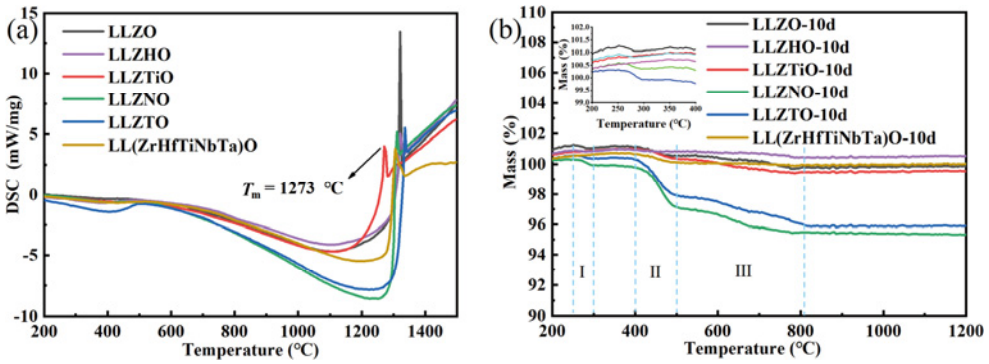

Fig. 9 (a) Thermal response in garnet powders during heating at 10 ℃/min. (b) TGA curves of garnet powders after 10 d exposed to air.

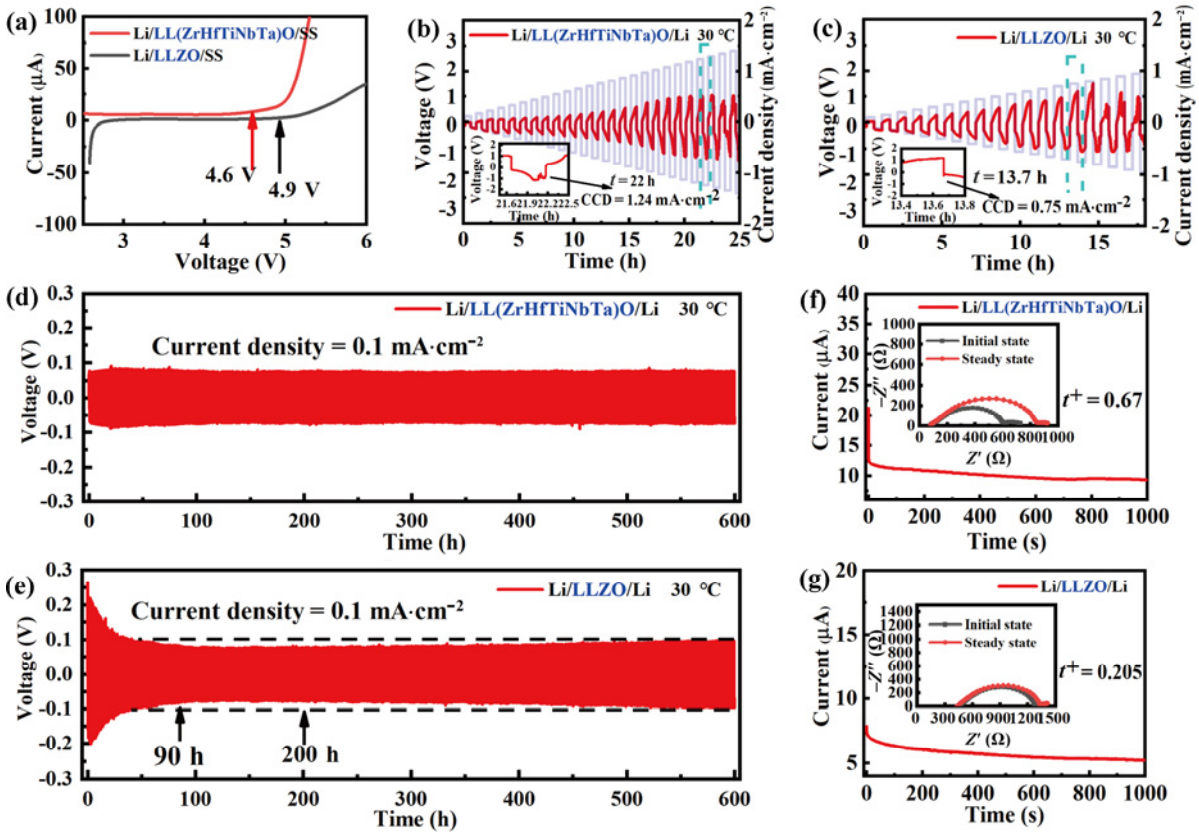

Fig. 10 (a) LSV curves of Li/LL(ZrHfTiNbTa)O/SS and Li/LLZO/SS cells. (b, c) CCDs of Li/LL(ZrHfTiNbTa)O/Li and Li/LLZO/Li cells, respectively (the insets are the micro short circuit). Galvanostatic cycling performance of (d) Li/LL(ZrHfTiNbTa)O/Li and (e) Li/LLZO/Li cells under current density of 0.1 mA/cm^2 at 30 ℃. Current–time curves of (f) Li/LL(ZrHfTiNbTa)O/Li and (g) Li/LLZO/Li symmetric cells at 10 mV of polarization (the insets display the EIS curves in initial and steady states).

noticeably improved from 0.75 to 1.24 mA/cm^2, meaning that the LL(ZrHfTiNbTa)O/Li interface is more stable than the LLZO/Li one (Figs. 10(b) and 10(c), respectively). It is worth noting that Ti is a redox element that can be easily reduced when contacting with a Li metal [49]. As shown in Fig. S8(a) in the ESM, a reduction peak appeared at a voltage of 1.15 V, possibly due to the reduction of Ti. In addition, XPS was used to analyze the valence change of Ti after cycling in the Li/LL(ZrHfTiNbTa)O symmetric cells. However, because of the small amount of Ti, no significant changes are observed (Fig. S8(b) in the ESM). According to a galvanostatic cycling curve (Figs. 10(d) and 10(e)), the Li/LL(ZrHfTiNbTa)O/Li cell maintained its stable cycling over 600 h with a plateau of ~70 mV at a current density of 0.1 mA/cm^2 and a temperature of 30 ℃. Thus, the stable and smooth Li^+ transport in the Li/LL(ZrHfTiNbTa)O/Li cell was demonstrated. On the contrary, the Li/LLZO/Li cell exhibited a large polarization potential and a rapid voltage drop, reaching cycling stability in 90 cycles. Then the polarization voltage slowly increased again after cycling for 200 h. This was attributed to the growth of lithium dendrites and the dissolution of lithium. Meanwhile, no lithium dendrites and morphology changes are observed in the LL(ZrHfTiNbTa)O pellet (Figs. S9(a) and S9(b) in the ESM). In contrast, there is lithium dendrite proliferation in the LLZO pellet (Fig. S9(c) and S9(d) in the ESM). As an important parameter for evaluating ion migration capability, Li^+ TN was measured by the modified Bruce–Vincent–Evans (BVE) method [50]. The Li^+ TN value of LL(ZrHfTiNbTa)O is 0.67 while being lower (0.205) in LLZO (Figs. 10(f) and 10(g), respectively), which suggested that LL(ZrHfTiNbTa)O had better ion migration capability and lower polarization.

Figure 11 shows charge/discharge curves and discharge-specific capacities for the Li/LL(ZrHfTiNbTa)O/LFP full cell at 30 ℃ with various rates. The cell displayed good rate capability with a low polarization

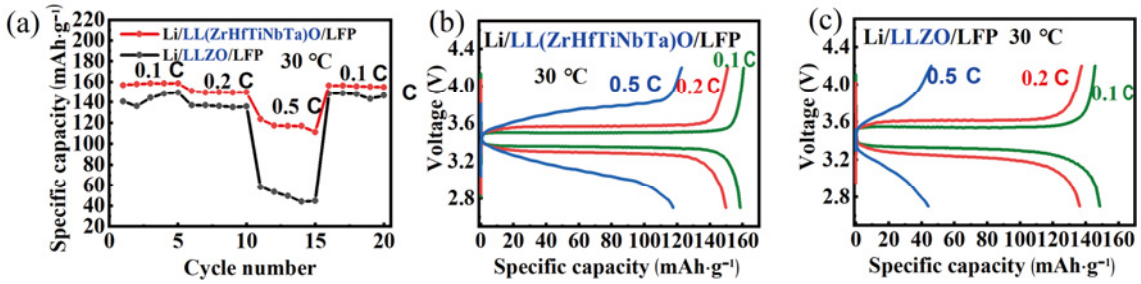

Fig. 11 (a) Rate performances of Li/LLZO/LFP and Li/LL(ZrHfTiNbTa)O/LFP full cells. (b, c) Charge/discharge curves of Li/LL(ZrHfTiNbTa)O/LFP and Li/LLZO/LFP cells at various rates, respectively.

voltage, delivering the discharge-specific capacity of 159, 150, and 117 mAh/g at various rates of 0.1, 0.2, and 0.5 C, respectively. However, the discharge capacity of the Li/LLZO/LFP cell could only reach 49 mAh/g at a rate of 0.5 C. Table S3 in the ESM displays the discharge capacities obtained in this work and recently reported values. All the results show that the HEG electrolytes synthesized by the authors have a promising application prospect in the solid-state batteries.

3. 5 Mechanical properties of LL(ZrHfTiNbTa)O pellet

Figure S10 in the ESM depicts Vickers hardness of the LL(ZrHfTiNbTa)O and LLZO pellets, which were approximately 980 and 555 MPa, respectively. Therefore, the high entropy was conducive to the enhancement in mechanical strength of LLZO due to its lattice distortion effect [18]. Moreover, it has been shown that high mechanical strength can suppress the growth of lithium dendrites [51]. Because of the above, high-entropy SSEs seem to be an optimal strategy for suppressing the lithium dendrite growth in new-generation devices.

4 Conclusions

In summary, HEG SSEs were produced by introducing five equimolar elements into the Zr site of the LLZO pellet through the solid-state reaction method. The ionic conductivity, surface morphology, and phase changes of the LL(ZrHfTiNbTa)O and LLZO pellets were tested for over 30 d. The ionic conductivity of LL(ZrHfTiNbTa)O remained unchanged for 60 d, and no Li_2CO_3 impurities were formed within 10 d. The results show the outstanding air stability of the LL(ZrHfTiNbTa)O composition compared to that of LLZO. We investigate the role of different elements and find that Hf can inhibit the exchange process of H^+/Li^+ to improve the air stability. Moreover, the LL(ZrHfTiNbTa)O electrolyte has a higher ion migration number than LLZO, and the related Li/LL(ZrHfTiNbTa)O/Li symmetric cell exhibited the cycling stability for more than 600 h. Also, the $LiFePO_4$/LL(ZrHfTiNbTa)O/Li cell shows excellent rate performance at 30 ℃. Therefore, it is shown that HEG SSEs have broad application prospects in the future.

Acknowledgements

This work was funded by the Central Government Guides Local Science and Technology Development Special Fund Projects (Grant No. YDZJSX2022B003), the Shanxi Province Science and Technology Major Projects (Grant No. 202101120401008), the Key Research and Development Project of Shanxi Province (Grant No. 202102030201006), and Science and Technology Activities of Overseas Students Merit-based Funding Projects of Shanxi Province (Grant No. 2021037).

Declaration of competing interest

The authors have no competing interests to declare that are relevant to the content of this article.

Electronic Supplementary Material

Supplementary material is available in the online version of this article at https://doi.org/10.26599/JAC.2023.9220749.

References

[1] Gonzalez Puente PM, Song SB, Cao SY, *et al*. Garnet-type solid electrolyte: Advances of ionic transport performance and its application in all-solid-state batteries. *J Adv Ceram* 2021, **10**: 933–972.

[2] Zhang SS. Liquid electrolyte lithium/sulfur battery: Fundamental chemistry, problems, and solutions. *J Power Sources* 2013, **231**: 153–162.

[3] Sun CW, Liu J, Gong YD, *et al*. Recent advances in all-solid-state rechargeable lithium batteries. *Nano Energy* 2017, **33**: 363–386.

[4] Wang CH, Liang JW, Hwang S, *et al*. Unveiling the critical role of interfacial ionic conductivity in all-solid-state lithium batteries. *Nano Energy* 2020, **72**: 104686.

[5] He LC, Oh JAS, Chua JJJ, *et al*. Synthesis and interface modification of oxide solid-state electrolyte-based all-solid-state lithium-ion batteries: Advances and perspectives. *Funct Mater Lett* 2021, **14**: 2130002.

[6] Tian HQ, Liu S, Deng LJ, *et al*. New-type Hf-based NASICON electrolyte for solid-state Na-ion batteries with superior long-cycling stability and rate capability. *Energy Storage Mater* 2021, **39**: 232–238.

[7] Gao JX, Wu JE, Han SY, *et al*. A novel solid electrolyte formed by NASICON-type $Li_3Zr_2Si_2PO_{12}$ and poly(vinylidene fluoride) for solid state batteries. *Funct Mater Lett* 2021, **14**: 2140001.

[8] Zhang BK, Yang LY, Wang LW, *et al*. Cooperative transport enabling fast Li-ion diffusion in thio-LISICON $Li_{10}SiP_2S_{12}$ solid electrolyte. *Nano Energy* 2019, **62**: 844–852.

[9] Li YT, Xu HH, Chien PH, *et al*. A perovskite electrolyte that is stable in moist air for lithium-ion batteries. *Angew Chem Int Ed* 2018, **57**: 8587–8591.

[10] Murugan R, Thangadurai V, Weppner W. Fast lithium ion conduction in garnet-type $Li_7La_3Zr_2O_{12}$. *Angew Chem Int Ed* 2007, **46**: 7778–7781.

[11] Thangadurai V, Narayanan S, Pinzaru D. Garnet-type solid-state fast Li ion conductors for Li batteries: Critical review. *Chem Soc Rev* 2014, **43**: 4714–4727.

[12] Huo HY, Luo J, Thangadurai V, *et al*. Li_2CO_3: A critical issue for developing solid garnet batteries. *ACS Energy Lett* 2020, **5**: 252–262.

[13] Ma C, Rangasamy E, Liang CD, *et al*. Excellent stability of a lithium-ion-conducting solid electrolyte upon reversible Li^+/H^+ exchange in aqueous solutions. *Angew Chem Int Ed* 2015, **54**: 129–133.

[14] Abrha LH, Hagos TT, Nikodimos Y, *et al*. Dual-doped cubic garnet solid electrolytes with superior air stability. *ACS Appl Mater Interfaces* 2020, **12**: 25709–25717.

[15] Hofstetter K, Samson AJ, Dai JQ, *et al*. Electrochemical stability of garnet-type $Li_7La_{2.75}Ca_{0.25}Zr_{1.75}Nb_{0.25}O_{12}$ with and without atomic layer deposited-Al_2O_3under CO_2 and humidity. *J Electrochem Soc* 2019, **166**: A1844–A1852.

[16] Jia MY, Bi ZJ, Shi C, *et al*. Air-stable dopamine-treated garnet ceramic particles for high-performance composite electrolytes. *J Power Sources* 2021, **486**: 229363.

[17] Wang CW, Xie H, Ping WW, *et al*. A general, highly efficient, high temperature thermal pulse toward high performance solid state electrolyte. *Energy Storage Mater* 2019, **17**: 234–241.

[18] Xiang HM, Xing Y, Dai FZ, *et al*. High-entropy ceramics: Present status, challenges, and a look forward. *J Adv Ceram* 2021, **10**: 385–441.

[19] Qin MD, Gild J, Hu CZ, *et al*. Dual-phase high-entropy ultra-high temperature ceramics. *J Eur Ceram Soc* 2020, **40**: 5037–5050.

[20] Sarker P, Harrington T, Toher C, *et al*. High-entropy high-hardness metal carbides discovered by entropy descriptors. *Nat Commun* 2018, **9**: 4980.

[21] Zhang Y, Jiang ZB, Sun SK, *et al*. Microstructure and mechanical properties of high-entropy borides derived from boro/carbothermal reduction. *J Eur Ceram Soc* 2019, **39**: 3920–3924.

[22] Gai JL, Zhao EQ, Ma FR, *et al*. Improving the Li-ion conductivity and air stability of cubic $Li_7La_3Zr_2O_{12}$ by the co-doping of Nb, Y on the Zr site. *J Eur Ceram Soc* 2018, **38**: 1673–1678.

[23] Geiger CA, Alekseev E, Lazic B, *et al*. Crystal chemistry and stability of "$Li_7La_3Zr_2O_{12}$" garnet: A fast lithium-ion conductor. *Inorg Chem* 2011, **50**: 1089–1097.

[24] Huang X, Xiu TP, Badding ME, *et al*. Two-step sintering strategy to prepare dense Li–garnet electrolyte ceramics with high Li^+ conductivity. *Ceram Int* 2018, **44**: 5660–5667.

[25] Miara LJ, Richards WD, Wang YE, *et al*. First-principles studies on cation dopants and electrolyte|cathode interphases for lithium garnets. *Chem Mater* 2015, **27**: 4040–4047.

[26] Abdulai M, Dermenci KB, Turan S. Lanthanide doping of $Li_7La_{3-x}M_xZr_2O_{12}$ (M = Sm, Dy, Er, Yb; x = 0.1–1.0) and dopant size effect on the electrochemical properties. *Ceram Int* 2021, **47**: 17034–17040.

[27] Xia WH, Xu BY, Duan HN, *et al*. Ionic conductivity and air stability of Al-doped $Li_7La_3Zr_2O_{12}$ sintered in alumina and Pt crucibles. *ACS Appl Mater Interfaces* 2016, **8**: 5335–5342.

[28] He X, Yan F, Gao MY, *et al*. Cu-doped alloy layer guiding uniform Li deposition on a Li–LLZO interface under high current density. *ACS Appl Mater Interfaces* 2021, **13**: 42212–42219.

[29] Zhao B, Ma WC, Li BB, *et al*. A fast and low-cost interface modification method to achieve high-performance garnet-based solid-state lithium metal batteries. *Nano Energy* 2022, **91**: 106643.

[30] Luo YL, Feng WW, Meng ZJ, *et al*. Interface modification in solid-state lithium batteries based on garnet-type electrolytes with high ionic conductivity. *Electrochim Acta* 2021, **397**: 139285.

[31] Tian Y, Zhou Y, Liu Y, *et al*. Formation mechanism of sol-gel synthesized $Li_{7-3x}Al_xLa_3Zr_2O_{12}$ and the influence of abnormal grain growth on ionic conductivity. *Solid State Ion* 2020, **354**: 115407.

[32] Fu KK, Gong YH, Liu BY, *et al*. Toward garnet electrolyte-based Li metal batteries: An ultrathin, highly effective, artificial solid-state electrolyte/metallic Li interface. *Sci Adv* 2017, **3**: e1601659.

[33] Qin MD, Yan QZ, Liu Y, *et al*. A new class of high-entropy M_3B_4 borides. *J Adv Ceram* 2021, **10**: 166–172.

[34] Im C, Park D, Kim H, *et al*. Al-incorporation into $Li_7La_3Zr_2O_{12}$ solid electrolyte keeping stabilized cubic

phase for all-solid-state Li batteries. *J Energy Chem* 2018, **27**: 1501–1508.

[35] Zheng YP, Zou MC, Zhang WY, *et al*. Electrical and thermal transport behaviours of high-entropy perovskite thermoelectric oxides. *J Adv Ceram* 2021, **10**: 377–384.

[36] Wang C, Liu ZG, Lin PP, *et al*. Liquid sintering of garnet electrolytes by lithium germanate: Properties and interfacial performance with lithium anode. *Appl Surf Sci* 2022, **575**: 151762.

[37] Huang X, Liu C, Lu Y, *et al*. A Li–garnet composite ceramic electrolyte and its solid-state Li–S battery. *J Power Sources* 2018, **382**: 190–197.

[38] Huang X, Wu LB, Huang Z, *et al*. Characterization and testing of key electrical and electrochemical properties of lithium-ion solid electrolytes. *Energy Stor Sci Technol* 2020, **9**: 479–500. (in Chinese)

[39] Kumazaki S, Iriyama Y, Kim KH, *et al*. High lithium ion conductive $Li_7La_3Zr_2O_{12}$ by inclusion of both Al and Si. *Electrochem Commun* 2011, **13**: 509–512.

[40] Du FM, Zhao N, Li YQ, *et al*. All solid state lithium batteries based on lamellar garnet-type ceramic electrolytes. *J Power Sources* 2015, **300**: 24–28.

[41] Zhang C, Hu XC, Nie ZW, *et al*. High-performance Ta-doped $Li_7La_3Zr_2O_{12}$ garnet oxides with AlN additive. *J Adv Ceram* 2022, **11**: 1530–1541.

[42] Hayashi A, Masuzawa N, Yubuchi S, *et al*. A sodium-ion sulfide solid electrolyte with unprecedented conductivity at room temperature. *Nat Commun* 2019, **10**: 5266.

[43] Huo HY, Chen Y, Zhao N, *et al*. *In-situ* formed Li_2CO_3-free garnet/Li interface by rapid acid treatment for dendrite-free solid-state batteries. *Nano Energy* 2019, **61**: 119–125.

[44] Huang L, Gao JA, Bi ZJ, *et al*. Comparative study of stability against moisture for solid garnet electrolytes with different dopants. *Energies* 2022, **15**: 3206.

[45] Chen X, Jia ZQ, Lv HM, *et al*. Improved stability against moisture and lithium metal by doping F into Li_3InCl_6. *J Power Sources* 2022, **545**: 231939.

[46] Yow ZF, Oh YL, Gu WY, *et al*. Effect of Li^+/H^+ exchange in water treated Ta-doped $Li_7La_3Zr_2O_{12}$. *Solid State Ion* 2016, **292**: 122–129.

[47] Shi JY, Sun G, Li LP, *et al*. Fluorine substitution at the O-site imparts enhanced chemical stability for garnet-structured electrolytes. *ACS Energy Lett* 2023, **8**: 48–55.

[48] Bi ZJ, Huang WL, Mu S, *et al*. Dual-interface reinforced flexible solid garnet batteries enabled by *in situ* solidified gel polymer electrolytes. *Nano Energy* 2021, **90**: 106498.

[49] Li BY, Su QM, Zhang J, *et al*. Multifunctional protection layers via a self-driven chemical reaction to stabilize lithium metal anodes. *ACS Appl Mater Interfaces* 2021, **13**: 56682–56691.

[50] Jiang GS, Qu CZ, Xu F, *et al*. Glassy metal–organic-framework-based quasi-solid-state electrolyte for high-performance lithium-metal batteries. *Adv Funct Mater* 2021, **31**: 2104300.

[51] Huo HY, Chen YE, Luo J, *et al*. Rational design of hierarchical "ceramic-in-polymer" and "polymer-in-ceramic" electrolytes for dendrite-free solid-state batteries. *Adv Energy Mater* 2019, **9**: 1804004.